MDPI

Article

Metal-Doped NASICON/Polymer Composite Solid Electrolyte for Lithium Titania Anode in Lithium-Ion Batteries

Chien-Te Hsieh [1,2,*], Tzu-Shaing Cho [1], Jeng-Kuei Chang [3,4,5,*] and Jagabandhu Patra [3,4,*]

1   Department of Chemical Engineering and Materials Science, Yuan Ze University, Taoyuan 32003, Taiwan
2   Department of Mechanical, Aerospace, and Biomedical Engineering, University of Tennessee, Knoxville, TN 37996, USA
3   Hierarchical Green-Energy Materials (Hi-GEM) Research Center, National Cheng Kung University, 1 University Road, Tainan 70101, Taiwan
4   Department of Materials Science and Engineering, National Yang Ming Chiao Tung University, Hsinchu 30010, Taiwan
5   Department of Chemical Engineering, Chung Yuan Christian University, Taoyuan 32023, Taiwan
*   Correspondence: cthsieh@saturn.yzu.edu.tw (C.-T.H.); jkchang@nycu.edu.tw (J.-K.C.); jpatra@gs.ncku.edu.tw (J.P.)

Abstract: This study reports five types of metal-doped (Co, Cu, Sn, V, and Zr) NASICON-type $Li_{1.3}Al_{0.3}Ti_{1.7}(PO_4)_3$ (LATP)/polymer composite solid electrolytes (CSEs) enabling $Li_4Ti_5O_{12}$ (LTO) anodes to have high rate capability and excellent cycling performance. The high Li^+-conductivity LATP samples are successfully synthesized through a modified sol–gel method followed by thermal calcination. We find that the cation dopants clearly influence the substitution of Al for Ti, with the type of dopant serving as a crucial factor in determining the ionic conductivity and interfacial resistance of the solid electrolyte. The CSE containing poly(vinylidene fluoride-co-hexafluoropropylene) (PVDF-HFP), lithium bis(trifluoromethanesulfonyl)imide (LiTFSI), and Sn-LATP shows an ionic conductivity of 1.88×10^{-4} S cm^{-1} at ambient temperature. The optimum conductivity can be attributed to alterations in the lattice parameters and Li^+ transport pathways owing to Sn doping. The solid-state cell equipped with the LTO-supported CSE containing Sn-LATP fillers demonstrates both excellent high rate capability at 5 C (with a capacity retention of 86% compared to the value measured at 0.2 C) and superior cycling stability, maintaining high Coulombic efficiency (>99.0%) over 510 cycles. These findings indicate that the proposed CSE is highly promising for use in solid-state lithium batteries with desirable charge–discharge properties and high durability.

Keywords: cation doping; solid-state batteries; electrolyte conductivity; rate capability; cycle life

1. Introduction

The importance of lithium-ion batteries (LIBs) has been acknowledged over several decades; nevertheless, continuous endeavors persist to enhance both the performance and safety of LIBs. Meeting the demands of LIB applications, which span from miniaturized electronics and home appliances to light and heavy electric vehicles [1–4], necessitates achieving a high energy density and a high power density. The energy density of LIBs is directly dominated by the redox potential difference between the positive (cathode) and negative (anode) electrodes [5], as well as their capacities. Traditionally, graphite has been the favored material for LIB anodes. The primary advantage of graphite lies in its low intercalation potential (~0.1 V vs. Li^+/Li) and low cost [6]. Lithium titanate ($Li_4Ti_5O_{12}$, LTO) has emerged as a promising substitute for traditional graphite anode materials for LIBs. The LTO anode operates at a higher potential (~1.55 V vs. Li^+/Li), offering enhanced safety features due to the prevention of Li dendrite formation [7]. The LTO anode has demonstrated remarkable cycling stability owing to its minimal volume change during Li^+ intercalation/deintercalation. Additionally, LTO has exhibited superior stability at high

working temperatures and a greater rate capability compared to that of graphite anodes [8], which is favorable for the high-power performance of LIBs.

The utilization of conventional LIBs that incorporate organic liquid electrolytes (i.e., volatile and flammable carbonate electrolytes) poses the risk of thermal instability, leading to potential explosion and catastrophic fire [9,10]. Consequently, solid-state lithium batteries (SSLBs) are considered promising next-generation lithium batteries. Solid-state electrolytes (SSEs), chosen over their liquid counterparts, mitigate safety concerns, and, importantly, these electrolytes can be coupled with various anode and cathode materials with desirable potentials and capacities for LIBs [11–14]. SSEs can be broadly categorized into two types: solid polymer electrolytes (SPEs) and inorganic solid (i.e., ceramic) electrolytes (ISEs) [15,16]. The poor ionic conductivity, inferior mechanical properties, and inadequate oxidation stability limit the use of SPEs [15], while ISEs are usually fragile and challenging to fabricate, making them unsuitable for practical applications [16]. Composite solid electrolytes (CSEs), composed of a polymer phase, Li salt, and Li^+-conducting inorganic fillers, have become a promising alternative [17,18]. In CSEs, the polymer phase has good flexibility, plasticity, and wettability toward electrodes [19,20], while the ceramic filler imparts high Li^+ conductivity and boosts the mechanical strength to prevent electrode short-circuiting [21,22]. A CSE, thus, blends the merits of SPEs and ISEs, endowing SSLBs with desirable charge–discharge properties. In fact, inorganic filler materials play a crucial role in CSEs. Among various inorganic Li^+-conducting fillers, NASICON-type $Li_{1.3}Al_{0.3}Ti_{1.7}(PO_4)_3$ (LATP) [23] and garnet-type $Li_7La_3Zr_2O_{12}$ (LLZO) have received a considerable amount of attention due to their adequate Li^+ conductivity and good chemical stability [24]. LLZO is chemically stable against Li metal [25]. LATP possesses a significant advantage in terms of material synthesis and practical commercialization, considering the relatively low cost of the raw materials and fabrication process. The high stability of LATP against H_2O/O_2 allows the material preparation and handling to proceed in the ambient air [23,26].

The exploration of LTO-supported SSEs for SSLBs remains limited, with only a few studies delving into this topic. Investigating LTO-supported SSEs has the potential to yield significant advancement in SSLB performance. The integration of LTO as a supporting material for SSE can enhance the overall stability, rate capability, and cycling performance of the battery. Moreover, the adoption of LTO-supported SSEs may play a pivotal role in addressing the key challenges associated with SSLBs, including high interfacial resistance and high SSE thickness [27–29]. Exploring the properties offered by LTO-supported SSE can pave the way for the development of high-performance SSLBs characterized by improved safety and stability.

One approach to enhance the ionic conductivity of LATP-based SSEs is through element doping [30–33], which involves partially replacing Ti^{4+} ions with metal ions. The LATP framework can be modified by introducing foreign cations with different valence states and ion radii, which causes lattice distortion and enhances ionic conductivity. This present work aims to develop an efficient sol–gel synthesis method for producing metal-doped $Li_{1.3}Al_{0.3}(Ti_{1.7-x}M_x)(PO_4)_3$, where Ti is partially replaced by other elements (M) such as Co, Cu, Sn, V, and Zr with $x = 0.3$. These elements are the most common dopants for battery electrodes and solid electrolyte materials, and the systematic comparison of the doping effects in the LATP lattice has never been conducted. In the sol–gel process, anhydrous ethanol is used to prevent the hydrolysis of the Ti precursor (i.e., titanium (IV) butoxide) and shorten the reaction time. In this study, we develop CSEs incorporating various metal-doped LATP fillers within polymeric matrixes for application in SSLBs. The CSE consists of metal-doped LATP powder, poly(vinylidene fluoride-co-hexafluoropropylene) (PVDF-HFP), and lithium bis(trifluoromethanesulfonyl)imide (LiTFSI). Although some studies have utilized polyethylene oxide (PEO), PEO-based systems tend to crystallize at ambient temperature, which can hinder ionic transport. PVDF-HFP is preferred over PEO due to its superior electrochemical stability and processability, as well as its chemical and mechanical stability across a broader temperature range [34,35]. Furthermore, HFP serves as an amorphous phase promoter, offering ion channels that increase the ionic conductivity

of the electrolyte system [35]. We conduct a detailed investigation into the impact of these CSEs on the specific capacity, rate capability, and cycling stability of Li||CSE||LTO cells. The excellent compatibility of the CSEs with LTO anodes secures a robust battery structure with low internal resistance and superior capacity retention during extended cycling.

2. Experimental Section

2.1. Sol–Gel Synthesis of Metal-Doped LATP Powders

The sol–gel synthesis of metal-doped $Li_{1.3}Al_{0.3}(Ti_{1.7-x}M_x)(PO_4)_3$ was carried out by replacing Ti with other M elements, where $x = 0.3$ and M = Co, Cu, Sn, V, and Zr. The synthesis procedures for metal-doped LATP powders are outlined as follows. All reagents employed in this study are of an analytical grade. A $Ti(C_6H_9O)_4$ (Sigma-Aldrich (St. Louis, MO, USA)); purity: 97%) precursor was dissolved in anhydrous ethanol. Stoichiometric amounts of $LiNO_3$ (J.T. Baker (Phillipsburg, NJ, USA)); purity: 98%) and $Al(NO_3)_3 \cdot 9H_2O$ (Sigma-Aldrich; purity: 99.9%) were dissolved in a 0.2 M citric acid (Showa (Gyoda, Japan); purity: 99.5%) solution and stirred at 90 °C for 1 h to form a stable and clear solution. Simultaneously, various metal ions were separately introduced into the solution with a stoichiometric ratio of Ti:M (1.4:0.3), where M = Co, Cu, Sn, V, and Zr. The $Co(NO_3)_2$ (Alfa Aesar (Haverhill, MA, USA)); purity: 98%), $CuSO_4 \cdot 5H_2O$ (Alfa Aesar; purity: 98%), $SnCl_2$ (Alfa Aesar; purity: 99%), VCl_3 (Sigma-Aldrich; purity: 97%), and $ZrCl_4$ (Sigma-Aldrich; purity: 99.9%) precursors were used. Subsequently, step-wise citric acid addition was performed to maintain a molar ratio of citric acid to total metal ions at 4:1. After adding a saturated $NH_4H_2PO_4$ (Alfa Aesar; purity: 99.995%) solution in a stoichiometric amount, the pH value of the mixed solution was adjusted to 7 using $NH_3 \cdot H_2O$. After maintaining at 90 °C for 5 h, the solution became a homogeneous emulsion, which was then moved to an oven at 120 °C until a dry gel was produced. The obtained dry gel was heated to 180 °C for 4 h and then 250 °C for 5 h to proceed with pyrolysis. The metal-doped LATP samples were eventually calcined at 850 °C under air for 2 h, while the temperature ramping rate was 5 °C min^{-1}. Through ball-milling with a planetary mill (Fritsch Pulverisette 6 (Idar-Oberstein, Germany)) at 700 rpm for 90 min with 1 mm diameter ZrO_2 balls (the ball to LATP weight ratio is 1:15), highly refined metal-doped LATP particles were obtained. The resulting metal-doped LATP samples were designated as Co-LATP, Cu-LATP, Sn-LATP, V-LATP, and Zr-LATP, according to the type of dopants. Pristine LATP powder without any dopants was designated as 0-LATP for comparison.

2.2. Fabrication of CSEs on LTO Anode Sheets

Anode slurry was prepared by mixing 88 wt% LTO powder, 6 wt% PVDF binder, 4 wt% Super-P, and 2 wt% KS-6 (conducting agent) in *N*-methyl-2-pyrrolidone (NMP) solution. This slurry was casted onto Cu foil with a doctor blade and vacuum-dried at 90 °C for 12 h. The coating layer was ~100 μm in thickness. The LTO anode sheets were roll-pressed and then cut into the desired dimensions for battery assembly. To fabricate the LTO-supported CSEs, LiTFSI (Sigma-Aldrich; purity: 99.95%) and PVDF-HFP (Sigma; molecular weight: 400,000) were dissolved in NMP and stirred well to form a homogeneous solution. The metal-doped LATP powder was gradually added to the solution and the resulting slurry was uniformly dispersed through a planetary milling process with a rotation speed of 700 rpm for 1 h. The obtained CSE slurry was then coated onto the LTO anode sheet using a doctor blade. The sheets were subjected to drying at 140 °C under vacuum overnight to form LTO-supported CSE samples. The thickness of the CSE layers was ~40 μm.

2.3. Material and Electrochemical Characterizations

The morphology of the metal-doped LATP samples was analyzed using field-emission scanning electron microscopy (FE-SEM; Zeiss ULTRA 55 (White Plains, NY, USA)) and transmission electron microscopy (TEM; FEI Talos F200s (Hillsboro, OR, USA)). The sample crystallinity was examined using X-ray diffraction (XRD; Bruker D2 Phaser (Billerica, MA, USA)). For electrochemical property measurements of LTO-supported CSE samples, coin

cells of CR2032 type were utilized with Li metal foil as the counter electrodes. The coin cells were assembled in an argon-filled glove box (Innovation Technology Co., Ltd. (Hong Kong, China)), where both the moisture and oxygen content levels were maintained at ~0.1 ppm. The charge–discharge capacities, rate capability, and cycling stability were evaluated at ambient temperature. The durability of the cells was evaluated through repeated cycling at 0.2 C charging and 0.5 C discharging; once the capacity retention degraded to <80%, the testing was terminated. The internal resistance of the coin cells assembled with various LTO-supported CSEs was evaluated using electrochemical impedance spectroscopy (EIS; CH Instruments 608C (Bee Cave, TX, USA)) within a frequency range of 100 kHz to 10 mHz.

3. Results and Discussion

Figure 1a–f show the FE-SEM images of pristine and metal-doped LATP powders. A slight degree of agglomeration is apparent in the pristine and metal-doped LATP powders, indicating a tendency of the particles to cluster together to some extent without substantial interconnection. The images reveal that the particle sizes of the samples range from 1.2 to 2.5 μm. This size distribution reveals the decent homogeneity of the particles. Figure 1g exhibits the XRD patterns of various LATP powders, which were prepared using the citric-acid-assisted sol–gel synthesis route followed by thermal calcination. The XRD pattern of the pristine LATP sample aligns with the standard NASICON-type structure (i.e., rhombohedral lattice; Card No.: ICDD 00-035-0754) [36]. The major characteristic peaks at the diffraction angles of 20.8°, 24.5°, 29.7°, and 33.3° correspond to the crystalline planes of (104), (113), (024), and (116), respectively [37,38]. Notably, there is an absence of any impurity phase in this pristine LATP sample. The metal-doped LATP samples demonstrate the same rhombohedral structure, although a minor impurity phase of $AlPO_4$ [30,33] is observed for the V-LATP and Zr-LATP samples. This observation implies that the V and Zr dopants could easily cause lattice distortion, leading to the extraction of aluminum atoms from the lattice to form $AlPO_4$.
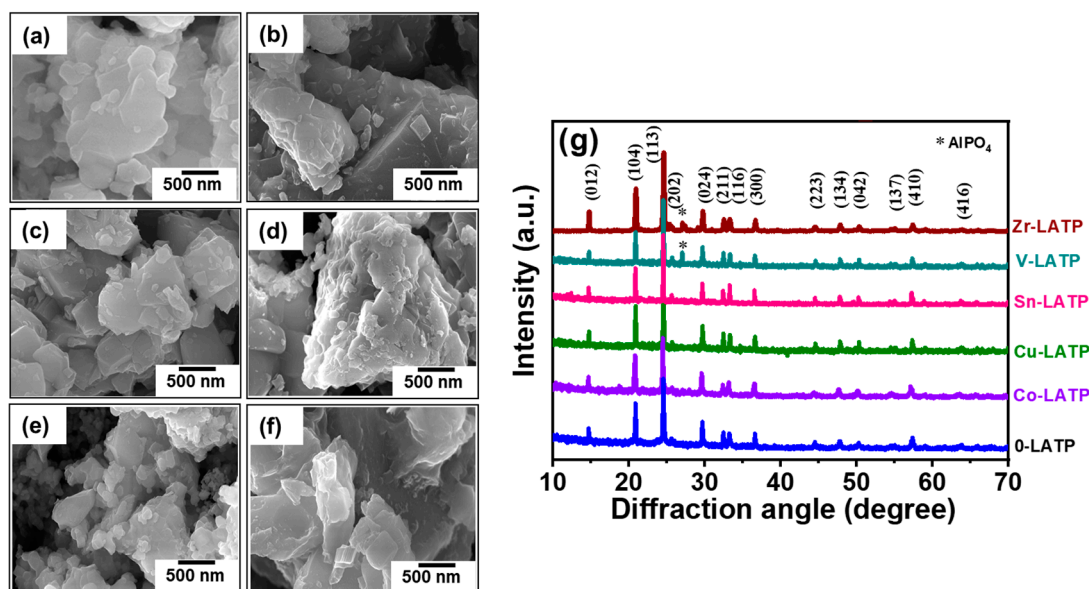

Figure 1. SEM images of (**a**) 0-LATP, (**b**) Co-LATP, (**c**) Cu-LATP, (**d**) Sn-LATP, (**e**) V-LATP, and (**f**) Zr-LATP samples. (**g**) XRD pattern of various samples synthesized.

Figure 2a,b illustrate the TEM micrographs of the Sn-LATP and Zr-LATP samples together with their elemental mapping data. Notably, these particles exhibit irregular morphology with a diameter of up to a few microns. Elements such as Al, Ti, P, and O are discernible across the metal-doped LATP samples. Of note, both the Sn and Zr dopants are uniformly dispersed within the particles. The energy-dispersive spectroscopy data also

confirmed that the M concentrations are 11.1 at%, 16.4 at%, 17.0 at%, 10.8 at%, and 11.5 at% for Co-LATP, Cu-LATP, Sn-LATP, V-LATP, and Zr-LATP samples, respectively.
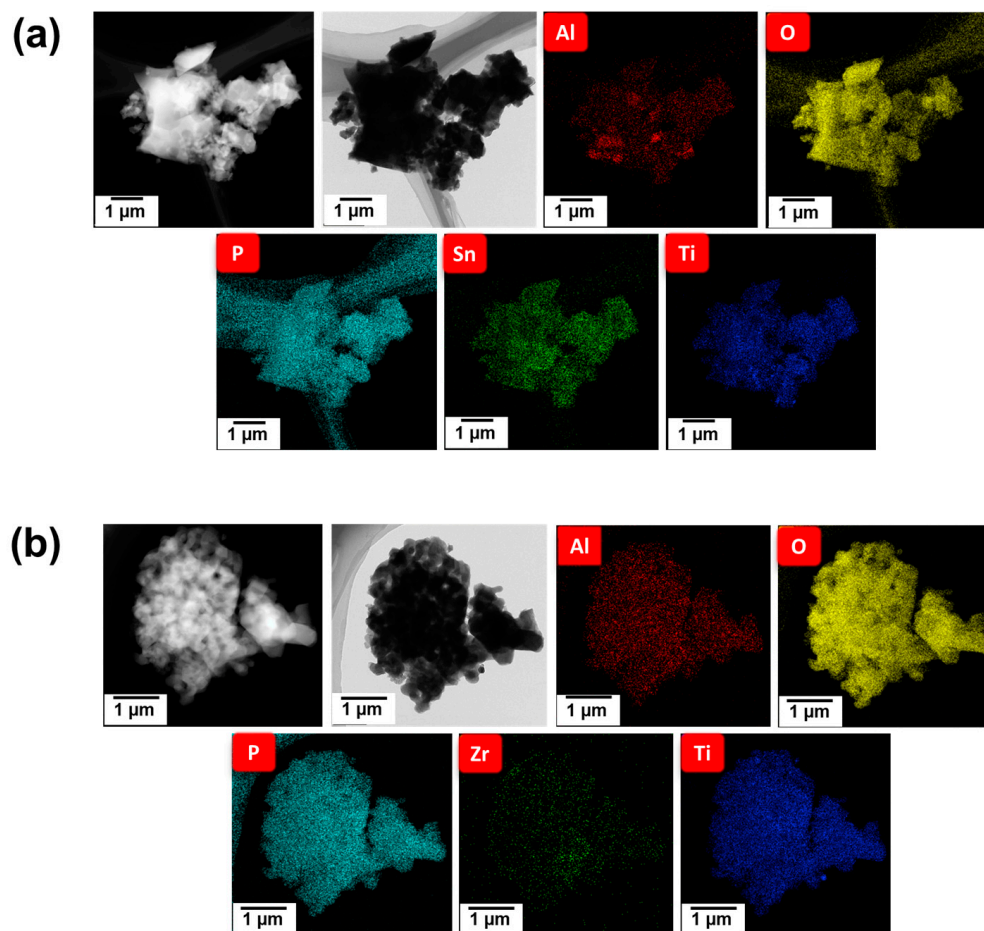

Figure 2. TEM micrographs of (**a**) Sn-LATP and (**b**) Zr-LATP samples and their corresponding elemental mapping data.

The oxidation states of Ti in the pristine and metal-doped LATP samples were investigated using X-ray photoelectron spectroscopy (XPS). The obtained data are shown in Figure 3. The two prominent peaks at approximately 459.6 and 465.5 eV correspond to Ti $2p_{3/2}$ and Ti $2p_{1/2}$, respectively [39,40]. As shown, for all of the LATP samples, Ti^{4+} is the major component, which is consistent with the literature [39–41]. However, two shoulder peaks at lower binding energies indicate the presence of Ti^{3+} [32,42]. The Ti^{4+}/Ti^{3+} ratios for various samples do not show significant difference. The high-resolution Co 2p, Cu 2p, Sn 3d, V 2d, and Zr 3d spectra for the Co-, Cu-, Sn-, V-, and Zr-LATP samples are shown in Figure 4. The Co 2p spectrum (Figure 4a) shows Co $2p_{3/2}$ and Co $2p_{1/2}$ signals [43]. Two satellite peaks are at 788.7 and 805.6 eV. The data show the coexistence of Co^{2+} and Co^{3+}. The Cu 2p spectrum (Figure 4b) shows two spin-orbital signals of Cu $2p_{3/2}$ and Cu $2p_{1/2}$ [44]. The co-existence of Cu^{+} and Cu^{2+} are confirmed. The two satellite peaks of Cu $2p_{3/2}$ are centered at 940.0 and 944.6 eV, respectively. In the Sn 3d spectrum (Figure 4c), the peaks at 487.7 eV (Sn $3d_{5/2}$) and 496.1 eV (Sn $3d_{3/2}$) belong to Sn^{4+} [45]. Figure 4d shows the characteristic peaks at 518.3 and 525.5 eV, which are ascribed to V $2p_{3/2}$ and V $2p_{1/2}$ of V^{5+}, respectively [46]. The Zr 3d spectrum in Figure 4e shows the characteristic signals of Zr $3d_{5/2}$ and Zr $3d_{3/2}$ at 185.8 and 183.6 eV, respectively. Both peaks belong to Zr^{4+} [47]. The data confirm that the cations are indeed doped in the LATP lattice.
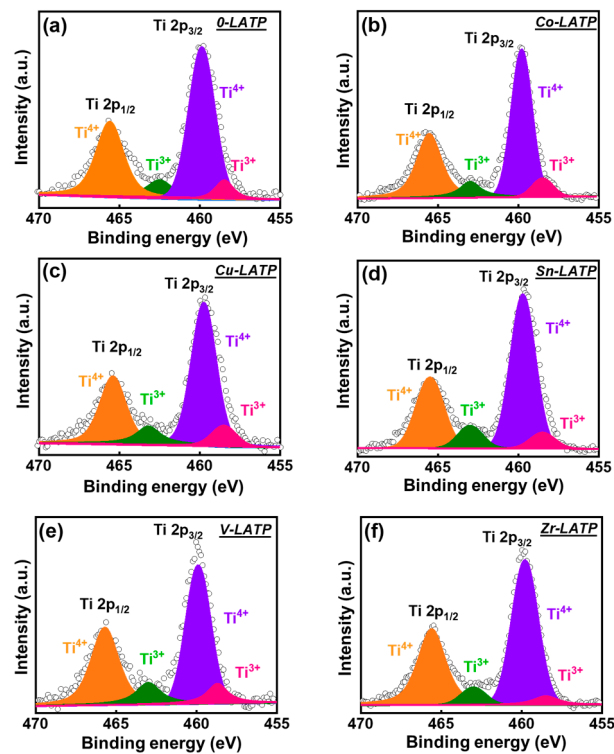
Figure 3. High-resolution XPS Ti 2p spectra of (**a**) 0-LATP, (**b**) Co-LATP, (**c**) Cu-LATP, (**d**) Sn-LATP, (**e**) V-LATP, and (**f**) Zr-LATP samples.
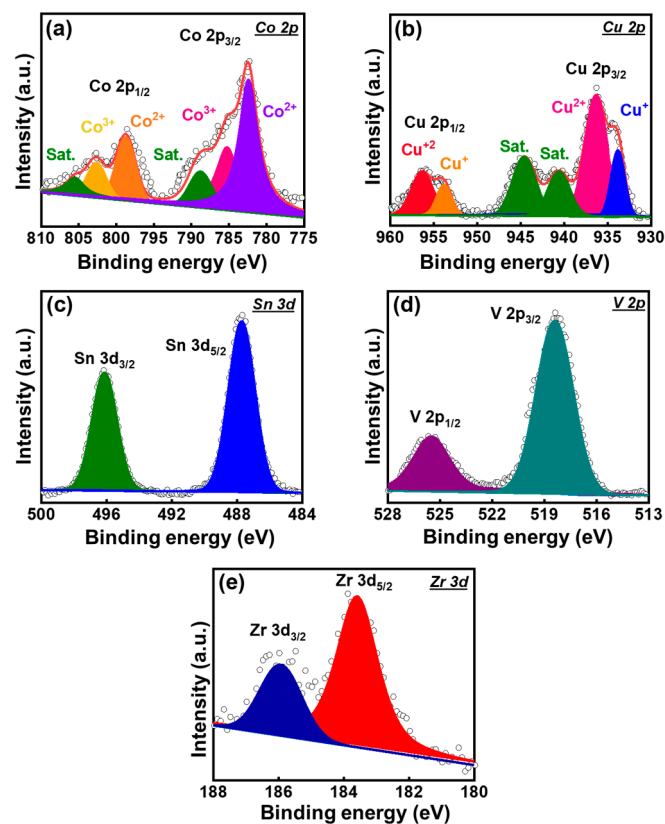

Figure 4. High-resolution XPS (**a**) Co 2p, (**b**) Cu 2p, (**c**) Sn 3d, (**d**) V 2p, and (**e**) Zr 3d spectra for Co-LATP, Cu-LATP, Sn-LATP, V-LATP, and Zr-LATP samples, respectively.

The EIS measurements were carried out with Li||CSE||LTO cells and conducted at ambient temperature in a frequency range of 100 kHz to 10 mHz. The representative data and the equivalent circuit used to fit the data are shown in Figure S1 (supporting information). The equivalent series resistance (ESR = resistance of bulk electrolyte + electrolyte/electrode interfacial resistance + charge-transfer resistance) was assessed to determine the overall internal resistance of the cells [48]. As shown in Figure 5a, the ESR values of the cells exhibit a strong dependence on the type of dopant. The order of ESR values is as follows: Zr -LATP (296 Ω) > Co-LATP (274 Ω) > Cu-LATP (240 Ω) > 0-LATP (215 Ω) > V-LATP (198 Ω) > Sn-LATP (195.5 Ω). These results highlight that the ESR value, representing the overall cell resistance, is significantly reduced for the cells containing the Sn-LATP and V-LATP CSEs.
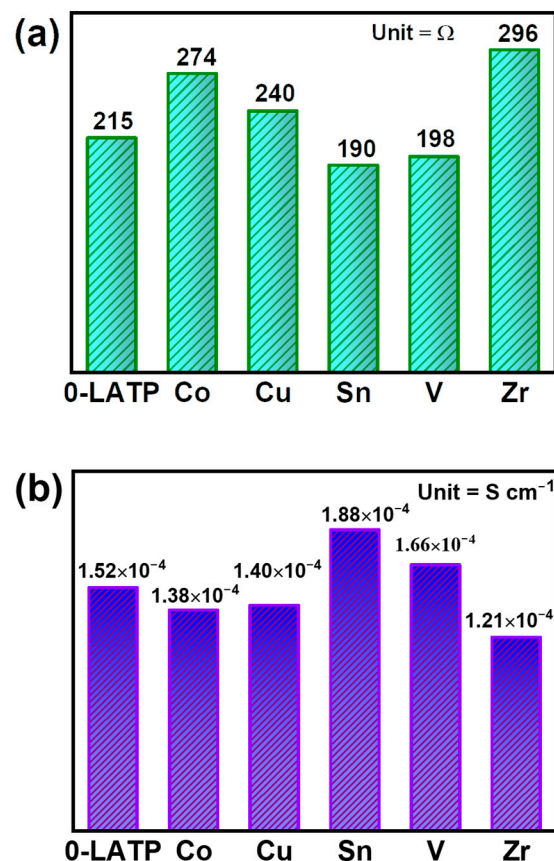

Figure 5. (**a**) ESR values of various Li||CSE||LTO cells. (**b**) Li$^+$ conductivity values of various types of CSE.

The ionic conductivity (σ) of various CSEs can be quantified to clarify the effects of the design of LATP powders by utilizing the high-frequency impedance (R) obtained from the EIS analysis. The ionic conductivity is determined using the formula $\sigma = l/(R \times A)$, where l is the thickness of the CSE and A is the projected area [49,50]. This calculation allows for the evaluation of the ionic conductivity of various CSEs. As depicted in Figure 5b, the σ values of the CSE samples follow the order of Sn-LATP (1.88×10^{-4} S cm^{-1}) > V-LATP (1.66×10^{-4} S cm^{-1}) > 0-LATP (1.52×10^{-4} S cm^{-1}) > Cu-LATP (1.40×10^{-4} S cm^{-1}) > Co-LATP (1.38×10^{-4} S cm^{-1}) > Zr-LATP (1.21×10^{-4} S cm^{-1}). These results highlight the clear improvement in ionic conductivity achieved through the chemical composition design of the ceramic fillers. As compared to the σ value of the LATP-0 sample, the Sn and V dopants in the LATP lattice show positive effects in increasing the ionic conductivity of the CSEs. Numerous factors influence the ionic conductivity of the doped LATP, including the dopant size, electronegativity, lattice volume, Li$^+$ concentration, lattice vacancies, and the interactions with the polymer phase [42,51,52]. Consequently, it is challenging to

precisely determine which factor dominates the conductivity of Sn-LATP at the current stage. Although we have experimentally examined the order of conductivity, the exact causes and underlying mechanisms for the superior conductivity observed still require further investigation.

The experimental results presented above indicate that the metal dopants for LATP play a significant role in enhancing the ionic conductivity of the solid electrolyte. Nevertheless, a more comprehensive investigation is needed to further understand how dopants such as Sn and V contribute to the improvement in Li$^+$ conduction in the LATP lattice. Theoretically, three primary Li$^+$ migration mechanisms in the crystal may be involved: (i) the ion migrating directly from one lattice site to a neighboring vacant site, (ii) the ion migrating from one site to a neighboring metastable vacant site through an interstitial site, and (iii) the ion migrating into a neighboring metastable vacant site followed by the occupation of its original site by an ion from the neighboring metastable site [53]. Based on these migration mechanisms, the Sn and V dopants are likely to create vacant sites (or grain boundaries), promoting ionic migration in the lattice and thereby enhancing Li$^+$ conductivity. This leads to a unique ion transport mechanism where Li$^+$ ions hop from one coordinating site to another, facilitated by the movement of defect sites, similar to the studies reported previously [12,54,55]. Figure 6 illustrates the bonding structures of Li-Co, Li-Cu, Li-Sn, and Li-Zr with the corresponding formation energies, as programmed by The Materials Project [56–58]. Particularly noteworthy is the most negative formation energies of the Li-Sn bonding structure (i.e., −0.326 eV/atom), indicating the most favorable formation relative to their bonds. This suggests that the Li$^+$ conducting pathways are relatively easy to form for Sn-LATP, leading to its superior ionic conductivity.
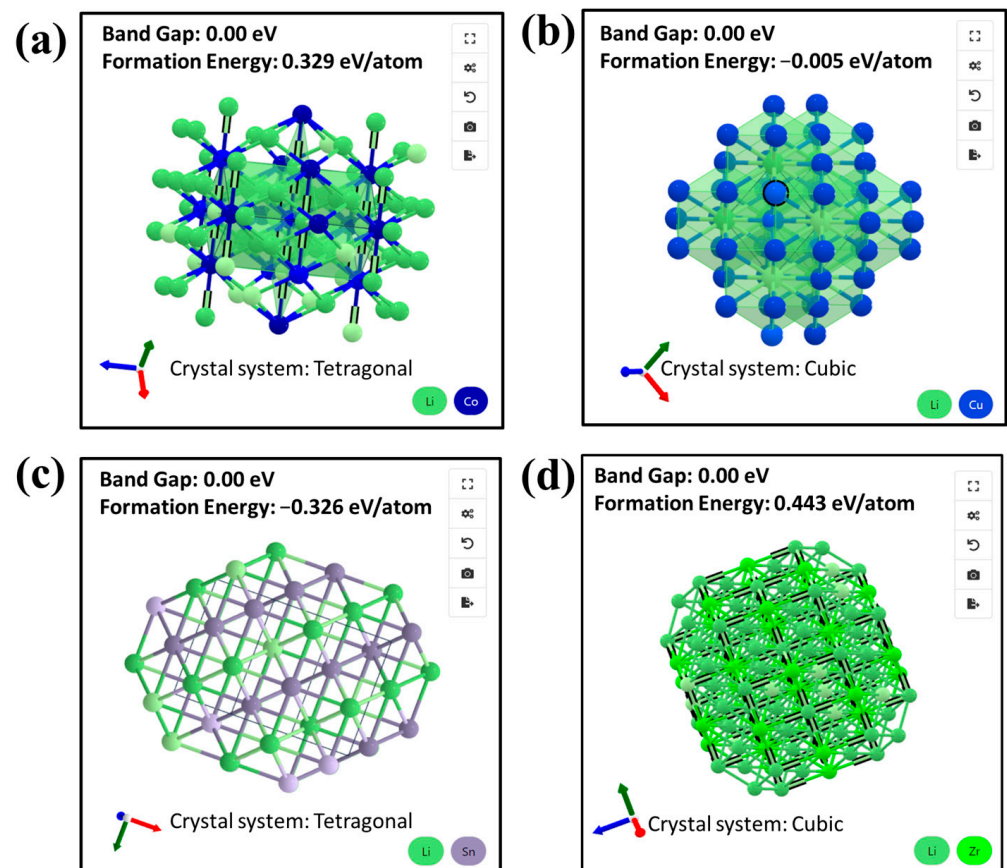

Figure 6. Schemes of bonding structures of (**a**) Li-Co, (**b**) Li-Cu, (**c**) Li-Sn, and (**d**) Li-Zr systems and their corresponding formation energies.

The charge–discharge profiles of the LTO half cells equipped with the CSEs containing 0-LATP and Sn-LATP are shown in Figure 7a,b, respectively. The charging and discharging tests were carried out within a voltage range of 0.5 to 2.8 V (vs. Li/Li$^+$) at different rates ranging from 0.2 to 5 C. At 0.2 C, the cells exhibit distinct voltage plateaus, signifying a two-phase reversible reaction at approximately 1.5 V vs. Li/Li$^+$. The intercalation/de-intercalation process can be expressed as [7] $Li_3[LiTi_5{}^{4+}]O_{12} + 3\,e^- + 3\,Li^+ \leftrightarrow Li_6[LiTi_3{}^{3+}Ti_2{}^{4+}]O_{12}$. During the electrode lithiation process, the Li ions insert into the octahedral (16c) sites of $Li_4Ti_5O_{12}$ lattices, forming a rock-salt structure [8]. Theoretically, a typical LTO electrode offers a reversible capacity of 175 mAh g^{-1}, based on the Li$^+$ insertion/de-insertion process mentioned above. Figure 7c compares the rate capability of various cells across the range of 0.2–5 C. As evident from the plot, all of the LTO electrodes exhibit high specific capacities of ~170 mAh g^{-1} at 0.2 C, very close to the theoretical value. At a high rate of 5 C, the cells with CSEs containing 0-LATP, Co-LATP, Cu-LATP, Sn-LATP, V-LATP, and Zr-LATP fillers showed reversible capacities of 120, 76, 85, 146, 131, and 38 mAh g^{-1}, respectively, corresponding to 70%, 44%, 49%, 86%, 77%, and 23% capacity retention compared to the values measured at 0.2 C. When the current rate decreased back to 0.2 C, the capacities were restored, as shown in Figure 7c. The cells equipped with the CSEs containing Sn-LATP and V-LATP demonstrated superior rate capability owing to the relatively low ESR and high Li$^+$ conductivity of the electrolyte layers. This promising outcome (i.e., high electrode performance at high rate) underscores that the LTO-supported CSEs have paved the way for realizing a high-power SSLB.
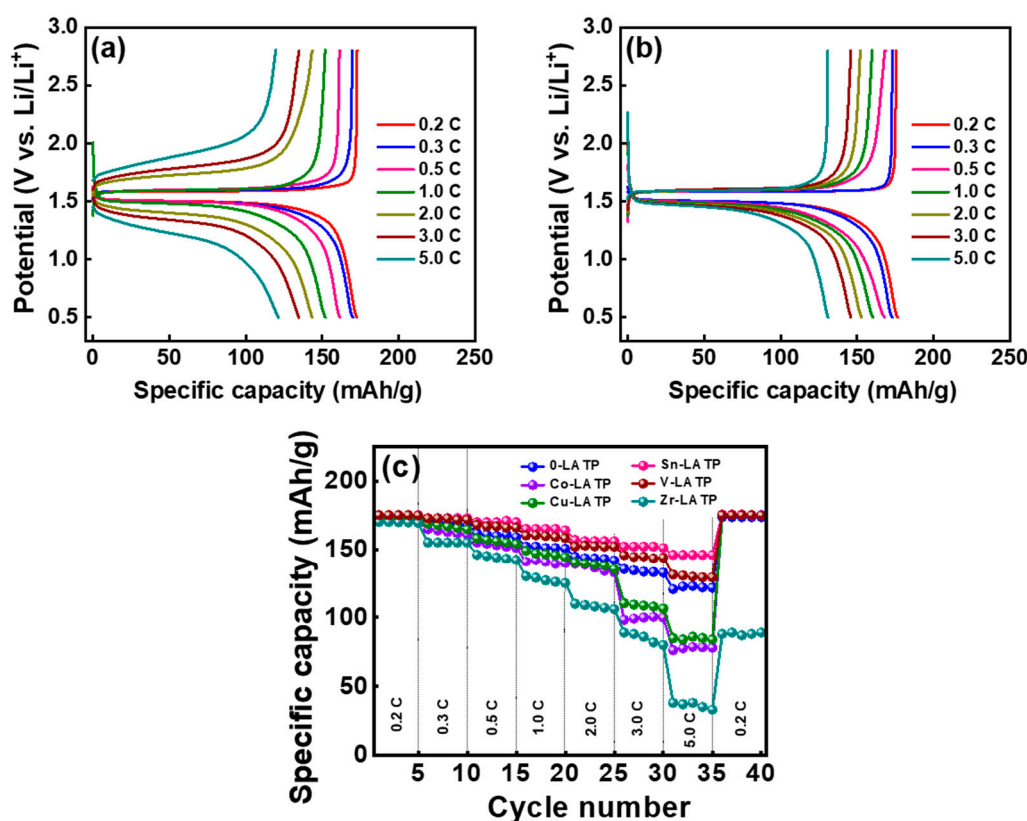

Figure 7. Charge–discharge curves of LTO half cells equipped with (**a**) 0-LATP and (**b**) Sn-LATP CSEs. (**c**) Comparative rate performance of various cells.

Figure 8a,b compare the charge–discharge curves of the LTO cells equipped with the CSEs containing 0-LATP and Sn-LATP fillers, respectively. The objective of this experiment was to assess the electrochemical stability of the cells through galvanostatic cycling at ambient temperature. An observable plateau at ~1.5 V and stable discharge performance upon cycling for the Sn-LATP cell reflect the robustness of the CSE layer. In addition,

the high reversibility of Li$^+$ intercalation and de-intercalation into/from the spinel LTO structure was confirmed. Figure 8c shows the capacity retention and Coulombic efficiency as a function of cycle number for various LTO-supported CSE cells. These metrics serve as indicators to assess the cycling stability of the cells. The cycling tests continued until the capacity retention fell below 80%. Notably, all of the cells demonstrated acceptable durability, maintaining over 80% capacity after at least 170 cycles. The comparative analysis indicates that the cell durability ranks as follows: Sn-LATP (510 cycles) > V-LATP (450 cycles) > Co-LATP (275 cycles) > Zr-LATP (240 cycles) > Cu-LATP (200 cycles) > 0-LATP (170 cycles). Compared to other dopants, the ionic radius of Sn^{4+} (0.69 Å) is closer to that of Ti^{4+} (0.605 Å). Therefore, the crystal structure does not experience excessive lattice distortion [59]. Furthermore, Sn^{4+} with higher Pauling electronegativity (1.96) can improve the stability of the NASICON framework [42,59]. Consequently, the cell equipped with the Sn-LATP CSE demonstrated optimal performance and maintained high Coulombic efficiency (>99.0%) over 510 cycles. These data also reveal the potential of these CSEs for improved electrochemical stability against Li metal electrodes (since Li metal foil was used as the counter electrodes for the LTO-supported CSE cells). After cell testing, no cation reduction reaction is observed. This phenomenon is likely attributed to the presence of the polymer phase in the CSE. The polymer phase plays a crucial role in the system to encapsulate the LATP particles, thus forming a protective barrier that isolates the LATP particles from direct contact with the lithium metal. The ceramic fillers enhance the mechanical strength of the CSEs, acting as the capping layers to suppress Li dendrite formation. Sn doping in LATP has been confirmed as an agreeable strategy to improve the CSE performance, which is highly compatible with both Li metal and LTO electrodes, enabling superior rate capability and desirable cycling stability of the solid-state cell.
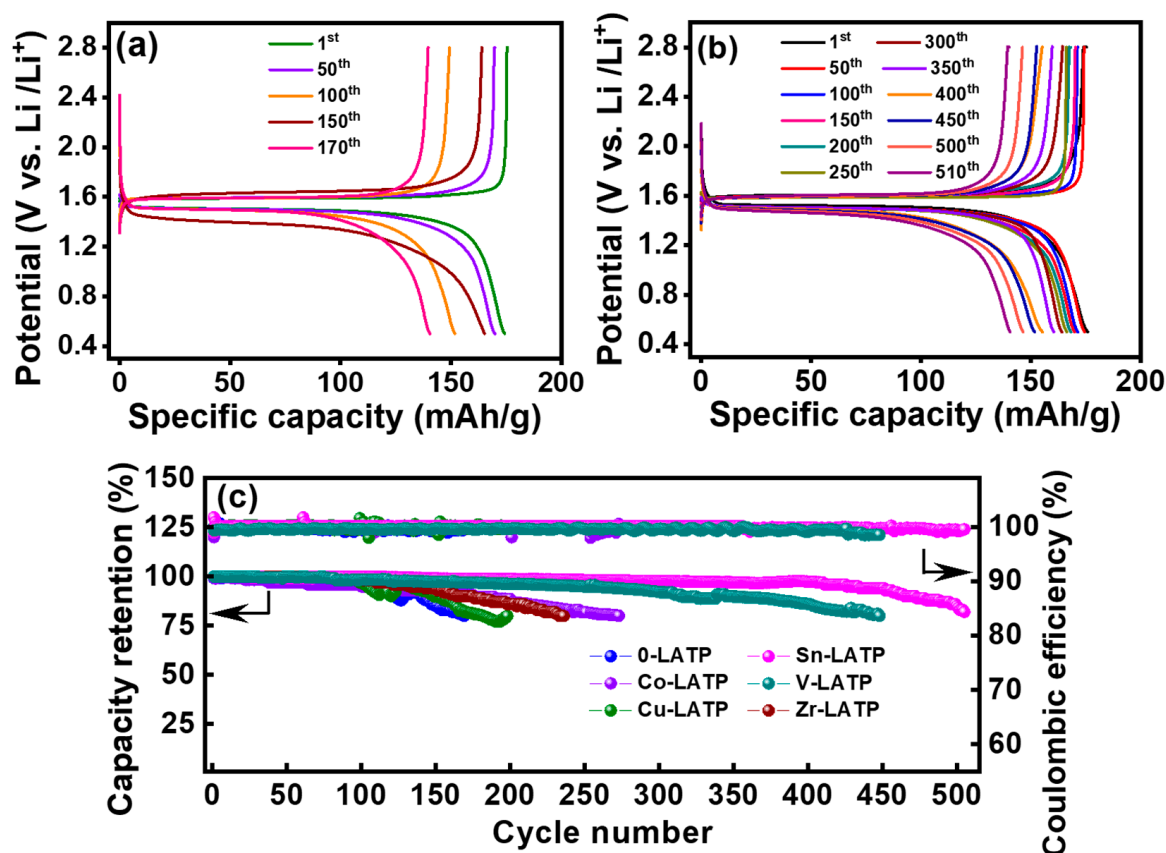

Figure 8. Charge–discharge curves of LTO half cells equipped with (**a**) 0-LATP and (**b**) Sn-LATP CSEs upon cycling. (**c**) Cycling stability data of various cells until capacity retention of 80%.

4. Conclusions

This study demonstrates the proper selection of metal-doped NASICON-type LATP SSE in enabling LTO anodes with high rate capability and great cycling performance. The Li$^+$-conducting LATP particles were successfully synthesized through a modified sol–gel method followed by thermal calcination. Five types of dopant (i.e., Co, Cu, Sn, V, and Zr) clearly influenced the substitution of Al for Ti, with the dopant type serving as a crucial factor in tuning the Li$^+$ conductivity and the ESR of the LTO-supported CSE cells. The CSE containing the Sn-LATP particles exhibited an ionic conductivity of 1.88×10^{-4} S cm^{-1} at ambient temperature. This enhanced conductivity could be attributed to the alteration in lattice parameters and the Li$^+$ transport pathways due to the Sn doping. The solid-state cell equipped with the LTO-supported CSE containing Sn-LATP fillers demonstrated both high rate capability at 5 C (with a capacity retention of 86% compared to the value measured at 0.2 C) and superior cycling stability, maintaining 80% of the initial capacity after 510 cycles. The close ionic radii of Sn^{4+} and Ti^{4+} prevent excessive lattice distortion, and the higher Pauling electronegativity of Sn^{4+} enhances the stability of the NASICON framework, leading to the optimal cell performance. These findings indicate that the CSE, composed of Sn-LATP ceramics, PVDF-HFP, and LiTFSI, is highly promising for use in SSLBs featuring high performance and high durability.

Supplementary Materials: The following supporting information can be downloaded at: https://www.mdpi.com/article/10.3390/polym16091251/s1, Figure S1: EIS data of Li||CSE (with 0-LATP)||LTO cell.

References

1. Arico, A.S.; Bruce, P.; Scrosati, B.; Tarascon, J.M.; van Schalkwijk, W. Nanostructured materials for advanced energy conversion and storage devices. *Nat. Mater.* **2005**, *4*, 366–377. [CrossRef] [PubMed]
2. Armand, M.; Tarascon, J.M. Building better batteries. *Nature* **2008**, *451*, 652–657. [CrossRef]
3. Patra, J.; Nguyen, T.X.; Tsai, C.C.; Clemens, O.; Li, J.; Pal, P.; Chan, W.K.; Lee, C.H.; Chen, H.Y.T.; Ting, J.M.; et al. Effect of elemental modulation on phase purity and electrochemical properties of Co-free high entropy spinel oxide anodes for lithium-ion batteries. *Adv. Funct. Mater.* **2022**, *32*, 2110992. [CrossRef]
4. Panda, A.; Patra, J.; Hsieh, C.T.; Huang, Y.C.; Gandomi, Y.A.; Fu, C.C.; Lin, M.H.; Juang, R.S.; Chang, J.K. Improving high-temperature performance of lithium-rich cathode by roll-to-roll atomic layer deposition of titania nanocoating for lithium-ion batteries. *J. Energy Storage* **2021**, *44*, 103348. [CrossRef]
5. Ghosh, A.; Ghamouss, F. Role of electrolytes in the stability and safety of lithium titanate-based batteries. *Front. Mater.* **2020**, *7*, 186. [CrossRef]
6. Sawai, K.; Iwakoshi, Y.; Ohzuku, T. Carbon materials for lithium-ion (shuttlecock) cells. *Solid State Ion.* **1994**, *69*, 273–283. [CrossRef]
7. Xu, G.; Han, P.; Dong, S.; Liu, H.; Cui, G.; Chen, L. Li$_4$Ti$_5$O$_{12}$-based energy conversion and storage systems: Status and prospects. *Coord. Chem. Rev.* **2017**, *343*, 139–184. [CrossRef]
8. Zhang, H.; Yang, Y.; Xu, H.; Wang, L.; Lu, X.; He, X. Li$_4$Ti$_5$O$_{12}$ spinel anode: Fundamental and advances in rechargeable batteries. *Infomat* **2022**, *4*, e12228. [CrossRef]
9. Chombo, P.V.; Laoonual, Y. A review of safety strategies of a Li-ion battery. *J. Power Sources* **2020**, *478*, 228649. [CrossRef]
10. Kalhoff, J.; Eshetu, G.G.; Bresser, D.; Passerini, S. Safer electrolytes for lithium-ion batteries: State of the art and perspectives. *ChemSusChem* **2015**, *8*, 2154–2175. [CrossRef]

11. Manthiram, A.; Yu, X.; Wang, S. Lithium battery chemistries enabled by solid-state electrolyte. *Nat. Rev. Mater.* **2017**, *2*, 16103. [CrossRef]

12. Sun, C.; Liu, J.; Gong, Y.; Wilkinson, D.P.; Zhang, J. Recent advances in all-solid-state rechargeable lithium batteries. *Nano Energy* **2017**, *33*, 363–386. [CrossRef]

13. Mishra, M.; Hsu, C.W.; Rath, P.C.; Patra, J.; Lai, H.Z.; Chang, T.L.; Wang, C.Y.; Wu, T.Y.; Lee, T.C.; Chang, J.K. Ga-doped lithium lanthanum zirconium oxide electrolyte for solid-state Li batteries. *Electrochim. Acta* **2020**, *353*, 136536. [CrossRef]

14. Tsai, Y.C.; Ku, M.C.; Hsieh, C.T.; Sung, P.Y.; Chen, P.S.; Mohanty, D.; Gandomi, Y.A.; Hung, I.M.; Patra, J.; Chang, J.K. Ceramicized NASICON-based solid-state electrolytes for lithium metal batteries. *J. Solid State Electrochem.* **2023**. [CrossRef]

15. Wang, H.; Sheng, L.; Yasin, G.; Wang, L.; Hong, X.; He, X. Reviewing the current status and development of polymer electrolytes for solid-state lithium batteries. *Energy Storage Mater.* **2020**, *33*, 188–215. [CrossRef]

16. Bachman, J.C.; Muy, S.; Grimaud, A.; Chang, H.H.; Pour, N.; Lux, S.F.; Paschos, O.; Maglia, F.; Lupart, S.; Lamp, P.; et al. Inorganic solid-state electrolytes for lithium batteries: Mechanism and properties governing ion conduction. *Chem. Rev.* **2016**, *116*, 140–162. [CrossRef]

17. Zheng, Y.; Yao, Y.; Ou, J.; Li, M.; Luo, D.; Dou, H.; Li, Z.; Amine, K.; Yu, A.; Chen, Z. A review of composite solid-state electrolytes for lithium batteries: Fundamentals, key materials and advanced structures. *Chem. Soc. Rev.* **2020**, *49*, 8790–8839. [CrossRef] [PubMed]

18. Rath, P.C.; Hsu, W.L.; Chen, C.C.; Huang, C.Y.; Wu, W.W.; Okada, S.; Dong, Q.F.; Yang, C.C.; Lee, T.C.; Chang, J.K. Dual interface design of Ga-doped $Li_7La_3Zr_2O_{12}$/polymer composite electrolytes for solid-state lithium batteries. *Int. J. Energy Res.* **2022**, *46*, 17693–17705. [CrossRef]

19. Yang, C.; Liu, B.; Jiang, F.; Zhang, Y.; Xie, H.; Hitz, E.; Hu, L. Garnet/polymer hybrid ion-conducting protective layer for stable lithium metal anode. *Nano Res.* **2017**, *10*, 4256–4265. [CrossRef]

20. Ding, W.Q.; Lv, F.; Xu, N.; Wu, M.T.; Liu, J.; Gao, X.P. Polyethylene oxide-based solid-state composite polymer electrolytes for rechargeable lithium batteries. *ACS Appl. Energy Mater.* **2021**, *4*, 4581–4601. [CrossRef]

21. Samson, A.J.; Hofstetter, K.; Bag, S.; Thangadurai, V. A bird's-eye view of Li-stuffed garnet-type $Li_7La_3Zr_2O_{12}$ ceramic electrolytes for advanced all-solid-state Li batteries. *Energy Environ. Sci.* **2019**, *12*, 2957–2975. [CrossRef]

22. Zhu, P.; Yan, C.; Dirican, M.; Zhu, J.; Zang, J.; Selvan, R.K.; Chung, C.C.; Jia, H.; Li, Y.; Kiyak, Y.; et al. $Li_{0.33}La_{0.557}TiO_3$ ceramic nanofiber-enhanced polyethylene oxide-based composite polymer electrolytes for all-solid-state lithium batteries. *J. Mater. Chem. A* **2018**, *6*, 4279–4285. [CrossRef]

23. Xiao, W.; Wang, J.; Fan, L.; Zhang, J.; Li, X. Recent advances in $Li_{1+x}Al_xTi_{2-x}(PO_4)_3$ solid-state electrolytes for safe lithium batteries. *Energy Storage Mater.* **2019**, *19*, 379–400. [CrossRef]

24. Xu, L.; Li, J.; Deng, W.; Shuai, H.; Li, S.; Xu, Z.; Li, J.; Hou, H.; Peng, H.; Zou, G.; et al. Garnet solid electrolytes for advanced all-solid-state Li batteries. *Adv. Energy Mat.* **2020**, *11*, 2000648. [CrossRef]

25. Shi, C.; Takeuchi, S.; Alexander, G.V.; Hamann, T.; Neill, J.O.; Dura, J.A.; Wachsman, E.D. High sulfur loading and capacity retention in bilayer garnet sulfurized-polyacrylonitrile/lithium-metal batteries with gel polymer electrolytes. *Adv. Energy Mater.* **2023**, *13*, 2301656. [CrossRef]

26. Yang, K.; Chen, L.; Ma, J.; He, Y.B.; Kang, F. Progress and perspective of $Li_{1+x}Al_xTi_{2-x}(PO_4)_3$ ceramic electrolyte in lithium batteries. *Infomat.* **2021**, *3*, 1195–1217. [CrossRef]

27. Zhou, Q.; Yang, X.; Xiong, X.; Zhang, Q.; Peng, B.; Chen, Y.; Wang, Z.; Fu, L.; Wu, Y. A solid electrolyte based on electrochemical active $Li_4Ti_5O_{12}$ with PVDF for solid-state lithium metal battery. *Adv. Energy Mater.* **2022**, *12*, 2201991. [CrossRef]

28. Cao, C.; Zhong, Y.; Chen, B.; Cai, R.; Shao, Z. A Li- $Li_4Ti_5O_{12}$ composite anode for reducing interfacial resistance of solid-state batteries. *Small Struct.* **2023**, *4*, 2200374. [CrossRef]

29. Cao, Y.; Li, Q.; Lou, S.; Ma, Y.; Du, C.; Gao, Y.; Yin, G. Enhanced electrochemical performance of $Li_4Ti_5O_{12}$ through in-situ coating $70Li_2S-30P_2S_5$ solid electrolyte for all solid-state lithium batteries. *J. Alloys Compd.* **2018**, *752*, 8–13. [CrossRef]

30. Kothari, D.H.; Kanchan, D.K. Effect of doping of trivalent cations Ga^{3+}, Sc^{3+}, Y^{3+} in $Li_{1.3}Al_{0.3}Ti_{1.7}(PO_4)_3$ (LATP) system on Li^+ ion conductivity. *Phys. Rev. B Condens.* **2016**, *501*, 90–94. [CrossRef]

31. Wang, R.; Chen, B.; Liu, C.; Yin, W.; Chen, H.; Zhang, J.; Zhang, T.; Sun, L.; Liu, X. Improving the ionic conductivity of $Li_{1+X}Al_XTi_{2-X}(PO_4)_3$ in a solid-state synthesis by regulating Li-O bond with B^{3+} and Y^{3+}. *J. Electrochem. Soc.* **2022**, *169*, 120535. [CrossRef]

32. Mashekova, A.; Baltash, Y.; Yegamkulov, M.; Trussov, I.; Bakenov, Z.; Mukanova, A. Polycation doping of the LATP ceramic electrolyte for Li-ion batteries. *RSC Adv.* **2022**, *12*, 29595–29601. [CrossRef] [PubMed]

33. Lu, X.; Li, Z.; Liu, S.; Huang, K.; Hai, J. Influence of rare-earth elements on the ionic conductivity of LATP electrolyte and its applications in assembled cells. *J. Am. Ceram. Soc.* **2024**, *107*, 2407–2420. [CrossRef]

34. Pradeepa, P.; Raj, S.E.; Sowmya, G.; Kalaiselvimary, J.; Prabhu, M.R. Optimization of hybrid polymer electrolytes with the effect of lithium salt concentration in PEO/PVDF-HFP blends. *Mater. Sci. Eng. B* **2016**, *205*, 6–17. [CrossRef]

35. Wu, F.; Zhang, K.; Liu, Y.; Gao, H.; Bai, Y.; Wang, X.; Wu, C. Polymer electrolytes and interfaces towards solid-state batteries: Recent advances and prospects. *Energy Storage Mater.* **2020**, *33*, 26–54. [CrossRef]

36. Luo, T.; Liu, B.; Han, W.; Zhu, G.; Liang, J.; Wang, L.; Yang, J.; Wang, L.; Liu, S. Enhanced ion-electron mixing interface for high energy solid-state lithium metal batteries. *J. Colloid Interface Sci* **2023**, *652*, 1085–1091. [CrossRef] [PubMed]

37. Shi, X.; Ma, N.; Wu, Y.; Lu, Y.; Xiao, Q.; Li, Z.; Lei, G. Fabrication and electrochemical properties of LATP/PVDF composite electrolyte for rechargeable lithium-ion battery. *Solid State Ion.* **2018**, *325*, 112–119. [CrossRef]

38. Shen, S.P.; Tang, G.; Li, H.J.; Zhang, L.; Zheng, J.C.; Luo, Y.; Yue, J.P.; Shi, Y.; Chen, Z. Low-temperature fabrication of NASICON-type LATP with superior ionic conductivity. *Ceram. Int.* **2022**, *48*, 36961. [CrossRef]

39. Wang, L.; Wang, L.; Shi, Q.; Zhong, C.; Gong, D.; Wang, X.; Zhan, C.; Liu, G. In-situ constructed SnO2 gradient buffer layer as a tight and robust interphase toward Li metal anodes in LATP solid-state batteries. *J. Energy Chem.* **2023**, *80*, 89–98. [CrossRef]

40. Wu, B.; Wang, S.; Lochala, J.; Desrochers, D.; Liu, B.; Zhang, W.; Yang, J.; Xiao, J. The role of the solid electrolyte interphase layer in preventing Li dendrite growth in solid-state batteries. *Energy Environ. Sci.* **2018**, *11*, 1803–1810. [CrossRef]

41. Wang, S.; Ding, Y.; Zhou, G.; Yu, G.; Manthiram, A. Durability of the $Li_{1+X}Ti_{2-X}Al_X(PO_4)_3$ solid electrolyte in Lithium-sulfur batteries. *ACS Energy Lett.* **2016**, *1*, 1080–1085. [CrossRef]

42. Wang, Q.; Liu, L.; Zhao, B.; Zhang, L.; Xiao, X.; Yan, H.; Xu, G.; Ma, L.; Liu, Y. Transport and interface characteristics of Te-doped NASICON solid electrolyte $Li_{1.3}Al_{0.3}Ti_{1.7}(PO_4)_3$. *Electrochim. Acta* **2021**, *399*, 139367. [CrossRef]

43. He, C.; Tao, J. 2D Co_6Mo_6C nanosheets as robust hydrogen evolution reaction electrocatalyst. *Adv. Sustain. Syst.* **2018**, *2*, 1700136. [CrossRef]

44. Chen, F.; Chen, C.; Hu, Q.; Xiang, B.; Song, T.; Zou, X.; Li, W.; Xiong, B.; Deng, M. Synthesis of CuO@CoNiLDH on Cu foam for high-performance supercapacitors. *Chem. Eng. J.* **2020**, *401*, 126145. [CrossRef]

45. Liu, X.; Najam, T.; Yasin, G.; Kumar, M.; Wang, M. One-pot synthesis of high-performance tin chalcogenides/C anodes for Li-ion batteries. *ACS Omega* **2021**, *6*, 17391–17399. [CrossRef] [PubMed]

46. Silversmit, G.; Depla, D.; Poelman, H.; Marin, G.B.; Gryse, R.D. Determination of the V 2p XPS binding energies for different vanadium oxidation states (V^{5+} to V^{0+}). *J. Electron Spectros. Relat. Phenomena* **2004**, *135*, 167–175. [CrossRef]

47. Liu, C.; Wang, X.; Xing, L.; Cheng, X.; Zhang, X.; Li, H.; Liu, M. Effect of Zr modification on NH_3-SCR reaction performance of Cu-Ce/SAPO-34 catalysts. *Appl. Sci.* **2023**, *13*, 4763. [CrossRef]

48. Mohammad, I.M.A.; Kanagaraj, P.; Yasin, A.S.; Iqbal, W.; Liu, C. Electrochemical impedance investigation of urea oxidation in alkaline media based on electrospun nanofibers towards the technology of direct-urea fuel cells. *J. Alloys Compd.* **2020**, *816*, 152513. [CrossRef]

49. Rath, P.C.; Jheng, Y.S.; Chen, C.C.; Tsai, C.L.; Su, Y.S.; Yang, C.C.; Eichel, R.A.; Hsieh, C.T.; Lee, T.C.; Chang, J.K. Tape-cast-Ce-substituted $Li_7La_3Zr_2O_{12}$ electrolyte for improving electrochemical performance of solid-state lithium batteries. *J. Mater. Chem. A* **2022**, *10*, 22512–22522. [CrossRef]

50. Chao, C.H.; Hsieh, C.T.; Ke, W.J.; Lee, W.L.; Lin, Y.F.; Liu, H.W.; Gu, S.; Fu, C.C.; Juang, R.S.; Mallick, B.C.; et al. Roll-to-roll atomic layer deposition of titania coating on polymeric separator for lithium ion batteries. *J. Power Sources* **2021**, *482*, 228896. [CrossRef]

51. Stenina, I.; Pyrkova, A.; Yaroslavtsev, A. NASICON-type $Li_{1.3}Al_{0.3}Ti_{1.7}(PO_4)_3$ solid electrolytes: Effect of Al, Zr, Co-doping and synthesis method. *Batteries* **2023**, *9*, 59. [CrossRef]

52. Zhu, Q.C.; Ma, J.; Huang, J.H.; Mao, D.Y.; Wang, K.X. Realizing long-cycling solid-state $Li-CO_2$ batteries using Zn-doped LATP ceramic electrolytes. *Chem. Eng. J.* **2024**, *482*, 148977. [CrossRef]

53. Famprikis, T.; Canepa, P.; Dawson, J.A.; Islam, M.S.; Masquelier, C. Fundamentals of inorganic solid-state electrolytes for batteries. *Nat. Mater.* **2019**, *18*, 1278–1291.

54. Gebert, F.; Knott, J.; Gorkin, R.; Chou, S.L.; Dou, S.X. Polymer electrolytes for sodium-ion batteries. *Energy Storage Mater.* **2021**, *36*, 10–30. [CrossRef]

55. Ratner, R.A.; Johansson, P.; Shriver, D.F. Polymer electrolytes: Ionic transport mechanisms and relaxation coupling. *MRS Bull.* **2000**, *25*, 31–37. [CrossRef]

56. Available online: https://next-gen.materialsproject.org/ (accessed on 28 April 2024).

57. Jain, A.; Ong, S.P.; Hautier, G.; Chen, W.; Richards, W.D.; Dacek, S.; Cholia, S.; Gunter, D.; Skinner, D.; Ceder, G.; et al. Commentary: The materials project: A materials genome approach to accelerating materials innovation. *APL Mater.* **2013**, *1*, 011002. [CrossRef]

58. Munro, J.M.; Latimer, K.; Horton, M.K.; Dwaraknath, S.; Persson, K.A. An improved symmetry-based approach to reciprocal space path selection in band structure calculations. *NPJ Comput. Mater* **2020**, *6*, 112. [CrossRef]

59. Xu, A.; Wang, R.; Yao, M.; Cao, J.; Li, M.; Yang, C.; Liu, F.; Ma, J. Electrochemical properties of an Sn-doped LATP ceramic electrolyte and its derived sandwich-structured composite solid electrolyte. *Nanomaterials* **2022**, *12*, 2082. [CrossRef]